Final Technical Report

Simulation of Three-Dimensional Ground Motion in Los Angeles From Earthquakes in Southern California

Award Number: 01-HQGR0040

Program Elements: I,II
January 1, 2001 to September 30, 2002

University of California at Santa Barbara
Office of Research
Santa Barbara, CA 93106
Cora Diaz

Dr. Kim B. Olsen, Principal Investigator

Institute for Crustal Studies
University of California at Santa Barbara
Santa Barbara, CA 93106-1100

September 30, 2002

Sponsored by the U.S. Geological Survey

Research supported by the U.S. Geological Survey (USGS), Department of the Interior, under USGS award number 01-HQ-PA-0002. The views and conclusions contained in this document are those of the authors and should not be interpreted as necessarily representing the official policies, either expressed or implied, of the U.S. Government.

AWARD#01HQGR0040 SIMULATION OF THREE DIMENSIONAL GROUND MOTION IN LOS ANGELES FROM EARTHQUAKES IN SOUTHERN CALIFORNIA

Dr. Kim B. Olsen, Institute for Crustal Studies, University of California at Santa Barbara, Santa Barbara, CA 93106-1100, phone: (805) 893 7394 (805), fax: 893 8649, email: kbolsen@crustal.ucsb.edu

Technical Abstract

I simulate 0-0.5 Hz 3D wave propagation through the Southern California Earthquake Center (SCEC) seismic velocity reference model, Version 2, for the 1994 Northridge earthquake in order to examine the effects of anelastic attenuation and amplification within the near-surface sediments. I use a fourth-order finite-difference (FD) staggered-grid method with the coarse-grained frequency-independent anelastic scheme of Day and Bradley (2001) and a variable slip distribution from kinematic inversion for the Northridge earthquake. I find that the near-surface material with S-wave velocity (V_s) as low as 500 m/s significantly affects the long-period peak ground velocities, compared with simulations in which the S-wave velocity is constrained to 1 km/s and greater. Anelastic attenuation also has a strong effect on ground motion amplitudes, reducing the predicted peak velocity by a factor of up to 2.5, relative to lossless simulations. Our preferred Q model is Q_s/V_s= 0.02 (V_s in m/s) for V_s less than 1-2 km/s, and much larger Q_s/V_s (0.1, V_s in m/s) for layers with higher velocities. The simple model reduces the standard deviation of the residuals between synthetic and observed natural log of peak velocity from 1.13 to 0.26, relative to simulations for the lossless case. The anelastic losses have their largest effect on short-period surface waves propagating in the Los Angeles basin, which are principally sensitive to Q_s in the low-velocity, near-surface sediments of the basin. The low-frequency ground motion simulated here is relatively insensitive to Q_p, as well as to the values of Q_s at depths greater than roughly that of the 2 km/s S-wave velocity isosurface.

The optimal Q model was used to construct site amplification maps for the Los Angeles basin for seven earthquake scenarios (M 6.75 earthquakes on the Palos Verdes, Elysian Park, Santa Monica, Newport-Inglewood faults, and approximations to the M 6.7 1994 Northridge, the M 6.4 1933 Long Beach, and the M 5.9 1987 Whittier-Narrows events), measured as 3D/1D 0-0.5 Hz peak velocity ratios. The individual scenarios show amplification of peak velocities up to an order of magnitude relative to the background model. The distribution of mean peak velocity ratios, as calculated from the seven scenarios, has a maximum of 5.1. In general, both the individual scenarios and their mean values show that the largest amplifications occur above the deepest parts of the basin and above the steeply-dipping basin boundaries. The largest mean amplification is furthermore associated with relatively small uncertainties. The largest uncertainties of the mean amplification above the basin (log standard deviation >1) are associated with sites in the southern part of the San Fernando Valley (SFV), northwest of SFV, and near Pasadena. For the seven scenario earthquakes, the amplification tends to increase with distance from the causative fault to the basin structure. It is possible that this pattern is due to stronger amplification of the more complex wavefield impinging onto the basin structure from the distant earthquakes compared to that of the predominant body waves from nearby earthquakes. The amplification is caused by a combination of effects from the 3D basin structure and differences in impedance between the 1D and 3D models. The maximum amplification averaged over sites above similar basin structure for the scenario earthquakes is 11.6, associated with sites located above the deeper part of the basin.

Non-Technical Abstract

Our numerical simulations suggest that ratios between local S-wave quality factors and S-wave velocities are as low as 0.02 for the Los Angeles basin, at least for material with S-wave velocities lower than 1-2 km/s. The most important effect of the attenuation model is in reducing the amplitudes of surface waves propagating within the basin sediments. Using this Q model I estimate site amplification for the Los Angeles basin using seven earthquake scenarios. The individual scenarios show amplification of peak velocities up to an order of magnitude relative to the background model, and mean peak velocity amplification has a maximum of 5.1. In general, both the individual scenarios and their mean values show that the largest amplifications occur above the deepest parts of the basin and above the steeply-dipping basin boundaries.

Introduction

Numerous studies have found that the three-dimensional elastic structure of sedimentary basins, such as the LA basin, causes strong amplification effects on earthquake ground motion. The wave propagation in the near-surface low-velocity material is likely to be heavily influenced by the anelastic attenuation. For example, the duration of shaking in alluvial valleys has been found to strongly depend on the anelastic attenuation (e.g., Olsen et al., 1995a). Recently, numerical simulations of ground motions have been extended from purely elastic computations (e.g., Olsen and Schuster, 1995; Olsen et al., 1995b; Olsen and Archuleta, 1996; Wald et al., 1996; Wald and Graves, 1998) to include approximations of anelastic loss. For example, Olsen (2000) found discrepancies generally less than a factor of two for 0.1-0.5 Hz synthetic and observed peak velocities from the 1994 M6.7 Northridge earthquake using only modest damping from the relations $Q_s = 0.1\ V_s$ (m/s) and $Q_p = 1.5\ Q_s$. However, all of these studies used an artificially high minimum S-wave velocity (V_s^{min}) of 1.0 km/s for the Los Angeles basin due to computational constraints. Such artificial exclusion of relatively low near-surface velocities may bias the estimates of Q which in turn may lead to biased ground motion predictions. Furthermore, those studies to date that have included anelastic losses have used simplified absorption models with unrealistic frequency dependence of Q.

Anelastic attenuation, here measured by the quality factor (Q), is relatively difficult to estimate *in situ*, in particular for sedimentary layers. Nevertheless, the variation of Q_s and Q_p has been documented for different kinds of sediments in several studies. Most of these studies include data from boreholes which may provide information on variations of Q related to variation in lithology. For example, Abercrombie (1997) found mean values of Q_p and Q_s of 24-106 and 17-52, respectively, increasing from the surface to the bottom of the Cajon, California, borehole (2900 m). Gibbs et al. (1994) found Q_s values of 10 and 15 in for Quaternary sediments at depth intervals 10-35 m and 40-115 m in the Santa Clara Valley, California. Wuncher et al. (1991) found Q_s of 22 in the upper 600 m of the Upper Mississippi Embayment. Hauksson et al. (1987) reported Q_p of about 44 throughout a 1500 m deep borehole penetrating Pleistocene and Pliocene sediments in the Newport-Inglewood fault zone, and a mean Q_s of 25 for the depth interval 420-1500 m. For the Garner Valley, Seale and Archuleta (1989) and Archuleta et al. (1992) published values of Q_s of 10 and 12, respectively for the upper 30 and 220 m of the soil, weathered granite, and granite encountered in their borehole array. Aster and Shearer (1991) reported Q_p and Q_s of 6.5 and 9, respectively, between 0 and 150 m, and 27 and 26, respectively, between 150 and 300 m in the San Jacinto fault zone, Anza, California. Jongmans and Malin (1995) found Q_s of 8, 8-12, and 65, respectively, at depth intervals 0-298 m, 298-572 m, and 572-938 m of Tertiary sediments at Parkfield, California. Malin et al. (1988) listed values of Q_s of 9 and 11 for depth intervals 0-475 m and 375-475 m, respectively, for Ophiolites in a borehole at Oroville, California. Finally, Wiggens et al. (1978) estimated the power law Q_s=$0.0053{V_s}^{1.25}$ (V_s in m/s) for San Onofre nuclear generating station. Most of these studies are based on frequencies higher than my target range of 0-0.5 Hz. However, since the Q of earth materials, in particular rock or consolidated sediments, is typically only weakly dependent upon frequency, the studies cited above may still be indicative of Q values to be expected for my frequency band (for more in-depth discussion of frequency-dependency of Q, see Sato and Fehler, 1998).

While most attenuation case studies have concentrated on estimating Q_s, a few have tried to estimate Q_p/Q_s. Abercrombie finds Q_p/Q_s of 1.4 to 2.0 from the surface towards the bottom of the Cajon borehole. Aster and Shearer (1991) find Q_p/Q_s of 0.72 for 0-150 m and 1.04 for 150-300 m for the San Jacinto fault zone. Chen et al. (1994) derive non-linear

Q_p-Q_s relations with $Q_s > Q_p$ if $Q_p <$ about 25 and $Q_s < Q_p$ if $Q_p >$ about 25.

In the present study I construct several simple distributions of Q_s and Q_p and identify those which provide the best fit between simulated and recorded 0-0.5 Hz peak velocities for the 1994 Northridge earthquake. Due to the relatively high levels of low frequency ground motion that it excited, the Northridge earthquake is a suitable source for estimation of Q for 0-0.5 Hz waves. Each Q structure tested has the form Q=f(V_s), with f piecewise linear. While physically, Q is not strictly a function of shear velocity, the quantities are usually strongly correlated. This approximation therefore provides a practical framework for parameterizing Q in ground motion simulations. Although I have not undertaken a comprehensive search for an optimal Q model, the estimates obtained here should suffice to significantly improve quantitative predictions of ground motion in the LA basin, and can serve as a starting point for more detailed studies of the regional Q structure. The preferred Q model is used to compute the response of the Los Angeles basin using the SCEC 3D velocity model and a regional 1D rock model (Hadley and Kanamori, 1977) for seven different earthquake scenarios. These scenarios are intended to reflect some of the variability of basin response for all sources of concern in the region. From the simulations I compute 3D/1D ratios of peak velocities.

Description of Basin Model, Earthquake Scenario, and Numerical Method

Basin Model

I use Version 2 of the Southern California Earthquake Center (SCEC) Reference Model (Magistrale et al., 2000) to represent the 3D seismic velocity and density structure of southern California. In the major sedimentary structures (Los Angeles basin, Ventura basin, San Gabriel Valley, San Fernando Valley, Chino basin, San Bernardino Valley, and the Salton Trough), the P-wave velocity estimates in the SCEC model are derived from sediments age and maximum depth of burial, following the empirical relationships of Faust (1951). Density and S wave velocity are derived from the P-wave estimate, using the empirical relations of Nafe and Drake (1960) and Ludwig et al. (1970). In crystalline basement rocks outside the basins, the velocities are determined from seismic tomography (Hauksson, 2000). Moho is represented in the model by a surface with the depths determined by the receiver function technique (Zhu and Kanamori, 2000). Shallow (less than $\approx$ 150 m) sediment S-wave velocities are interpolated from borehole S-wave measurements, with the aid of the site classification map of Wills et al. (2000).

Figure 1 shows the model area for the Northridge simulations. The 3D nature of the model is illustrated in Figure 2 by an isosurface corresponding to an S-wave velocity of 2.5 km/s. The large depression is the Los Angeles basin. The smaller basin to the northwest is located below the San Fernando Valley (SFV), separated from the Los Angeles basin by the Santa Monica Mountains, with the Ventura basin continuing to the North. A relatively small basin is located below the San Gabriel Valley (SGV), and the larger, but shallower Chino basin extends the LA basin to the East. Finally, the San Bernardino basin continues the Chino basin eastward to the San Andreas Fault (SAF). Note that the reference frame of the model in Figure 2 is rotated 32^o counterclockwise from North to minimize the computational requirements for the simulations. The axis of the main basin trends approximately 122^o as does the causative fault for the 1994 Northridge earthquake. Throughout this paper I use azimuths of 122^o and 32^o to analyze the horizontal ground motion for the earthquake simulations. The topography above sea level and ocean water are not included in the simulations.

Figure 3 shows depth contours for isosurfaces of (top) V_s=0.5 km/s and (bottom) V_s=1.0 km/s, respectively. The main LA basin is outlined by the 150 m depth contour for V_s = 0.5 km/s and the 850 m depth contour for V_s = 1.0 km/s. The maximum depths of the V_s = 0.5 km/s and V_s = 1.0 km/s isosurfaces are about 300 m and 1.3 km, respectively. In previous studies, volumes with V_s less than 1.0 km/s have been replaced by material with V_s equal to 1.0 km/s (e.g., Olsen, 2000; Wald and Graves, 1998). The large maximum depth extent of sediments with $V_s < 1.0$ km/s suggests that this velocity clamping, while necessary in previous ground motion studies due to computational limitations, may significantly bias the amplitudes, and therefore the estimate of Q. Here, I include sediments with V_s as low as 500 m/s. This model still assigns artificially high S-wave velocities to up to 300 m of near-surface sediments, as illustrated in Figure 3 (top). However, I have compared point source solutions in the SCEC model with solutions obtained by Bielak and Fernandez (personal communication), who used a finite element method permitting very fine discretization of the low-velocity layers. Based on these comparisons, I conclude that the neglect of velocities below 500 m/s in the SCEC model causes at most a small underestimate of amplitudes in the 0-0.5 Hz band, typically less than about 10-20%. As will be shown, this error is small compared with the amplitude overestimate caused by the neglect of anelastic attenuation.

Earthquake Scenario

I have selected the 1994 M 6.7 Northridge (NR) earthquake for our attenuation sensitivity study. This earthquake is well-recorded within the basin, with relatively good signal-to-noise ratio for frequencies below 0.5 Hz. For the slip distribution I use the combined kinematic inversion (i.e, the solution based upon teleseismic, strong motion, and geodetic data) of Wald et al. (1996), with a moment of $1.3 \cdot 10^{19}$ N m and an average rupture velocity of 3 km/s. The slip rate function of Wald et al. consists of three overlapping isosceles triangles, each with duration 0.6 sec. I simplify this slip rate function, using instead a single isosceles triangle with 1 sec duration, while preserving the total Wald et al. seismic moment estimate of each fault surface element. This simplification has little effect on the synthetic waveforms in the frequency range considered here. The source parameters are summarized in Table 1.

Numerical Method

The physical model is discretized with a grid spacing equivalent to 5 nodes per minimum shear wavelength of 1.0 km (i.e., the minimum V_s of 0.5 km/s divided by the maximum resolved frequency of 0.5 Hz). Our tests show that this rule-of-thumb commonly used for fourth-order schemes (e.g., Levander, 1988) provides sufficiently accurate peak velocities. The full model is discretized at 0.2 km grid spacing into 52.7 million grid points. The 3D modeling parameters are listed in Table 2. The source is implemented in the finite-difference grid by adding $M_{ij}^n(t)/dx^3$ to $S_{ij}^n(t)$ where $M_{ij}^n(t)$ is the $ijth$ component of the moment tensor contribution to the nth computational unit cell at time t, and $S_{ij}^n(t)$ is the $ijth$ component of the stress tensor in the nth cell at time t. The synthetic seismograms are lowpass filtered to frequencies less than 0.5 Hz (Butterworth filter with 4 poles and 2 passes). I use a staggered-grid finite-difference scheme to solve the 3D elastic equations of motion (Levander, 1988; Olsen et al., 1995a,b; Olsen and Archuleta, 1996; Graves, 1996); the accuracy is fourth-order in space and second-order in time. The numerical implementation of the 3D scheme is described in Olsen (1994). The media parameters are averaged spatially as suggested by Moczo et al. (2002),e.g., arithmetically for densities and harmonically for Lamé parameters. I use the absorbing boundary conditions of Clayton and Engquist (1977), and the sides of

the computational model are padded with homogeneous regions of attenuative material to furthermore limit reflections from the boundaries of the grid (Cerjan et al., 1985).

The ground motion simulations presented in the literature include various approximations of anelastic loss. Graves (1996) used an approximation where anelastic attenuation is applied in a form which is equivalent to a Maxwell solid (Q proportional to frequency) – without distinction between Q_s and Q_p. Olsen (2000) and Olsen et al. (2000) used the viscoelastic approach by Blanch et al. (1995) and Robertsson et al. (1994), using a standard linear solid model with one relaxation peak. However, Day (1998) and Day and Bradley (2001) significantly improved the accuracy of the stress relaxation schemes using a coarse-grained implementation of the memory variables, which is used in my analysis here. This implementation closely approximates frequency-independent Q by incorporating a large number of relaxation times (8 in my calculations) into the relaxation function, and does so without sacrifice of computational or memory efficiency.

Anelastic Attenuation in the Los Angeles Basin

Comparison to Data

I apply the above method to examine the effects of low sediment velocities and anelastic attenuation on ground motion in the 0-0.5 Hz range. Figure 4 shows comparisons between the natural log of the observed and synthetic horizontal peak velocities for data and synthetics from simulations of the Northridge earthquake using various distributions of Q_s and Q_p, at sites within the greater Los Angeles basin. I measure the horizontal peak velocity as $\sqrt{V_x \cdot V_y}$, where V_x and V_y are the maximum values of the absolute particle velocity time histories along 122^o and 32^o, respectively. The record length of the data varies between 30 and 60 s. However, due to uncertainties in the time correlation I do not attempt to determine the peak velocities from the synthetics for the time interval corresponding exactly to that for the data records. Instead, I assume that the true peak ground velocities were observed within the data records, and consistently compute the peak values for the synthetics from 120 s of simulated ground motion. This procedure introduces the risk of comparing weakly attenuated first-arrivals in the data and highly attenuated surface waves in the synthetics, or vice versa. However, at most stations, the peaks do occur at similar times in the synthetic and observed records, in particular for the surface waves at the LA Basin stations that are dominating the attenuation estimates.

Figure 4a-b compare the residuals obtained using minimum V_s values of 1 km/s (a) and 0.5 km/s (b), respectively, in lossless models. In both cases, the synthetic peak velocities overpredict the observations, particularly at deep basin sites, as would be expected due to the omission of finite Q in both simulations. However, the important point to be drawn from this comparison is that the simulated amplitudes are sensitive to the minimum V_s values, even in the relatively low-frequency band of 0-0.5 Hz which I are targeting here. In particular, the comparison shows that ${V_s}^{min}$ of 1 km/s is not low enough to accurately simulate an important feature of the seismograms at this frequency. Compared with using the lower ${V_s}^{min}$ of 0.5 km/s, the artificial 1 km/s clamp has an effect on peak velocity comparable in magnitude to the effect of anelastic attenuation that I are trying to model and quantify. In contrast, there are two lines of argument to suggest that the lower ${V_s}^{min}$ value, 0.5 km/s, is low enough to provide sufficient 0-0.5 Hz accuracy to support my objectives. The first is a comparison of two point-source finite element simulations done for the SCEC model (J. Bielak and A. Fernandez, personal communication, 2002), using ${V_s}^{min}$ values of 0.5 km/s and 0.2 km/s, respectively. Peak velocity differences between between these simulations are

typically less than 10-20%. A second supporting argument, based on the 1D RMS theory for the amplification of SH waves (Day, 1996), gives a very similar result. Starting with a model with V_s^{min} equal to 0.5 km/s, I apply Equation 37 of Day (1996), with an upper cutoff frequency (f_{max}) of 0.5 Hz, to gauge the effect of adding a 100-m thick near-surface layer with V_s of 300 m/s. This modification approximately follows the mean minus one σ LA basin profile in Magistrale et al., 2000, Figure 5. The low-velocity modification results in amplification of the peak velocity by a further factor of only $\approx$ 20%, compared with the model with V_s^{min} of 0.5 km/s.

Figure 4 (c-i) show results for V_s^{min}=0.5 km/s. In Figure 4c-e I explore the effect of anelastic attenuation on peak velocities for Q_s defined as fractions (0.1, 0.05, and 0.02, respectively) of V_s (m/s), compared to a loss-less model (Figure 4a). The peak velocities of the data are overpredicted in the main LA basin for $Q_s/V_s = \infty$, 0.1 and 0.05 but are in closer agreement for Q_s/V_s=0.02. The variation of Q_s for the Q_s/V_s relations used in Figure 4c-e are illustrated in Figure 5 at the deep basin site IGU (see Figure 6 for location). Q_s/V_s=0.02, 0.05, and 0.1 generate variations of Q_s at IGU between 10-50, 25-120, and 50-240 from the surface to a depth of 3 km, respectively. While $Q_s/V_s = 0.02$ provides a better overall comparison between synthetic and observed peak velocities, the fit at some basin and particularly rock sites in the Santa Monica Mountains and other areas surrounding the LA basin is degraded due to excessive damping. This underprediction is likely in part due to a relatively large uncertainty of the near-surface shear-wave velocities in the parts of the SCEC model lying outside the sedimentary basins. Other possible causes of the misfits include the omission of mountain topography and a realistic lateral shear impedance along the coastline. The inclusion of both of these features in the simulations is numerically challenging, but likely possible in future revisions of my results using more sophisticated simulation schemes.

It is possible that that Q_s/V_s ratio varies between layers with smaller and larger V_s. Intuitively, Q_s/V_s may be expected to be larger than 0.02 for layers with larger V_s, which is explored in Figure 4f-h. Here, I examine the effect of using Q_s/V_s=0.1 for V_s greater than a threshold value, V_s^T. The fit for the peak velocities using V_s^T=1.5 km/s and 2 km/s are similar to that for V_s^T=∞ (Figure 4d) while V_s^T=1 km/s generates overprediction in the NW part of the main LA basin.

Figure 4i examines the sensitivity of the peak values to Q_p. The comparison is made for V_s^T=2 km/s as in Figure 4h, but using $Q_p = Q_s(3/4)(V_p/V_s)^2$, which implies $Q(bulk) = \infty$. The fit to the peak velocities is almost identical to that for Q_p=1.5Q_s, suggesting that the peak velocities in the model are mostly insensitive to Q_p. This result is not surprising, considering an abundance of S and surface waves propagating in the LA basin for the Northridge event (Olsen, 2000).

The misfits in Figure 4 are quantified in Table 3 by the root mean square (RMS) of the natural log of the peak velocity residuals for two sets of sites, 14 deep basin sites from the main LA basin (locations are shown in Figure 4j) as well as for all 61 (rock and sediment) sites. I provide separate measurements of the misfit for the deep basin sites for two reasons. Firstly, the deep LA basin sediment sites are most sensitive to Q due to the importance of short-period surface waves at these sites, and the presence of relatively low near-surface S-wave velocities. Secondly, this set of sites excludes rock sites where there are relatively large uncertainties on the S-wave velocities in the current SCEC reference model (because the velocity function in those portions of the model lying outside the major basins is based on seismic tomography, which cannot resolve near-surface variations on the scale of the wavelength used in this study). The smallest RMS residuals are obtained from the simulations using Q_s/V_s of 0.02 for V_s <1-2 km/s for both sets of sites. If only one value of Q_s/V_s is used throughout the model (V_s^T=∞),

Q_s/V_s=0.05 provides a smaller log standard deviation compared to Q_s/V_s=0.02.

Figure 6 shows comparisons between recorded and simulated seismograms using Q_s/V_s of 0.02 for V_s < 1.5 km/s and Q_s/V_s=0.1 for V_s > 1.5 km/s, at thirteen stations for various distances and azimuths from the fault. The lossy model is also compared to the elastic model in Figure 6. For each station, the comparisons between the seismograms are made at the same scale for all three components and for the available record length of the data. Due to the lack of absolute timing the synthetic and recorded seismograms are aligned visually. The fits among the phases vary considerably. For all the simulations, the best results are obtained for stations located near the source, such as SSA (Santa Susanna) and JFP (Jensen Filtration Plant), but the phase agreement is degraded at larger distances from the fault, where the effects of model error become increasingly large. Note that the model fails to reproduce the large recorded velocity pulse on the horizontal component along 122^o at SMG (Santa Monica City Hall Grounds). The amplitudes of synthetics for the lossy model are seen to be decreased by up to a factor of 3 at some basin sites, compared to the purely elastic response, while the near-source synthetics are mostly insensitive to attenuation. The latter is expected from the predominantly short-duration body waves in the near field, and in agreement with the omission of Q in the kinematic slip inversion for the Northridge earthquake by Wald et al. (1996). From Figure 7, it appears that the effects of anelastic attenuation are most significant for relatively late-arriving, short-period ($\approx$ 2 sec) surface waves. This is reasonable, in that such waves would be expected to be highly sensitive to damping by shallow sediments. Figure 7 emphasizes this predominance of anelastic effects in the late-arriving surface waves by contrasting the model behavior at near-fault station JFP (Fig 7 top) with that at more distant LA Basin station IGU (Fig 7 bottom), over a long (125 s) record duration. The preferred Q model produces peak velocities only about 30% as large as does the lossless model at Inglewood (IGU). Similarly strong attenuation effects are present at other deep basin sites such as LBL and DOW. In contrast, at Jensen Filtration Plant (JFP), directly above the fault plane, the preferred synthetics have peaks about 94% of the lossless case.

Finally, Figure 8 shows the peak velocities from the simulation using Q_s/V_s of 0.02 for V_s < 1.5 km/s and Q_s/V_s=0.1 for V_s > 1.5 km/s. The largest peak velocities occur on the strike-perpendicular component (32^o), in the up-dip area just north of the fault where the directivity was most prominent, in agreement with data. The maximum 0-0.5 Hz peak velocities on the 122^o, 32^o, and vertical components were 70 cm/s, 167 cm/s, and 83 cm/s, respectively. These values are in agreement with those from data, where the largest broadband peak velocity (177 cm/s) was recorded in the Van Norman Complex of the San Fernando Valley (Bardet and Davis, 1996). The largest simulated peak velocities in the LA basin occur just south of the Santa Monica Mountains. In particular, the peak velocities are relatively large in Santa Monica, near the intersection of I10 and I405, which was damaged in the earthquake. Further south into the LA basin, attenuation has significantly reduced the ground motion.

Los Angeles Basin Amplification

I use ratios of 0-0.5 Hz horizontal peak velocities for the 3D SCEC Reference Velocity Model and the 1D model by Hadley and Kanamori (1977) throughout the rectangular area shown in Figure 2, similar to the approach by Olsen (2000). The 3D/1D ratios have the advantage of eliminating the geometrical spreading effects included in the 3D response and the 1D reference value for a given site. The conventional corrections for such effects using 1/r attenuation for body wave propagation can be misleading for traces that include strong surface waves. A disadvantage of the method is that artifacts may show up in the amplification maps

due to singularities in the rupture pattern. However, such effects are found to be small for the scenarios in this study. Note that the amplification patterns here are not corrected for the differences in velocities and densities between the two models in the area where the basin is located (lowest S-wave velocity is 2.7 km/s for the 1D model, 0.5 km/s for the 3D model).

Earthquake Scenarios

I have selected seven scenario earthquakes to calculate the basin amplification using the preferred attenuation model obtained above, namely a bilateral strike-slip rupture on the Palos Verdes fault (PV), blind thrust on the Elysian Park fault (EP), thrust on the Santa Monica fault (SM), northwest propagating rupture on the Newport-Inglewood fault (NI), and approximations of the 1994 M 6.7 Northridge (NR), 1933 M 6.4 Long Beach (LB), and 1987 M 5.9 Whittier-Narrows (WN) earthquakes (Table 1). These earthquakes are all within the "geological reasonable scenarios" defined by Dolan et al. (1995). The rupture velocity is 3 km/s for all finite fault scenarios, and rise time is 0.2 s for the Whittier Narrows earthquake, and 1 s for all remaining scenarios. All scenarios use a triangular slip rate function.

Scenario Amplification Maps

Figure 10 shows 3D/1D amplification values for the seven earthquake scenarios described above. Note that both the pattern and amplitudes of the amplification distributions for the seven scenarios vary considerably within the model area. While the deeper basin areas are generally characterized by increased 3D/1D ratios, some of the largest amplification tends to occur above the most steeply-dipping basin boundaries and the basin edges, similar to the results by Olsen et al. (1995a) for the Salt Lake Basin. This amplification is typically caused by the generation of surface waves at the basin edges, along with resonance in shallower sub-basins such as the SGV.

The largest basin amplification is obtained for the EP (24.7), NR (17.7) and WN (13.0) events (Figure 10). Compared to other events, the NR generates generally larger amplification above the basin. This pattern suggests that the amplification increases with distance from the causative fault to the basin structure. A possible reason for this pattern is that the larger-amplitude surface waves generated for the distant events, in part at the basin edges, are more prone to amplification than are the predominant body waves impinging onto the basin sediments from the nearby earthquakes. This interpretation is supported by evidence from the variability of Northridge aftershock ground motions in the San Fernando Valley (Hough et al., 1995), and is in agreement with Olsen (2000).

Mean LA Basin Amplification

In order to construct an amplification map for Los Angeles that combines the variations in fault location and rupture mechanism I have calculated the mean 0-0.5 Hz peak velocity ratios. The average, maximum values, and the standard deviation for the seven earthquake scenarios described above are shown in Figure 11. The LA and SGV basins generally show mean amplification above 3, with localized areas above 4, up to a maximum mean ratio of about 5. While some of the largest mean amplification occurs above the deepest part of the basin, considerable mean amplification is found near the edges of the LA basin as well as in the SGV. The overall largest amplifications (up to 25) occur near Inglewood, Downey, and Anaheim. The estimated standard deviation (of the natural-log amplification) shows generally lower values for larger mean amplification. For example, the standard deviation is

less than 1 at most sites where the total mean amplification is larger than 3. The largest uncertainties above the basin are found in the southern SFV, northwest of SFV, and near Pasadena. The large uncertainty in the southern SFV is due to strong amplification in this area from NR, SM and PV.

Amplification Versus Basin Depth

Another way of characterizing the basin amplification is to average values for sites located above similar velocity/density profiles in the basin. Here I choose to average the values for sites with common depth to the isosurface of 2.5 km/s. Figure 12 shows these values for the seven scenario earthquakes as well as the mean and log standard deviation. I have omitted values for depths larger than 6 km due to their limited number. The amplification generally increases gradually with increasing depth to the isosurface. The NR scenario is also responsible for the largest amplification values (up to about 11.6), as noted from the scenario amplification maps. The least amplification with depth is obtained for the SM, LB and PV scenarios. In fact, these and other scenarios generate de-amplification at shallow basin sites, caused by the transfer of energy from the initial arrivals to secondary phases in the 3D model. The mean amplification values for the scenarios as a function of depth to the isosurface gradually increase from 1 outside the basin to about 5 above the deepest part of the basin.

Discussion

The objective of the present study is to find a distribution of Q_s and Q_p as functions of V_s and V_p which provides an improved basis for practical ground motion simulations and a starting point for more detailed future studies of Q structure. From a series of trial-and-error simulations of the 1994 Northridge earthquake, I have found Q distributions that reduce the standard deviation of the residuals between observed and predicted log peak velocity from 1.13 to 0.26. It is likely that further improvement to the Northridge data fit could be obtained by a different parameterization of Q, or a more comprehensive search of the parameter space, or both. In addition, future studies should also seek to refine the Q model by using ground motion data from additional earthquakes that will sample the LA Basin model differently. Both types of refinement are beyond the scope of the present study.

The results of this study are obtained for relatively long-period waves (>2 s) propagating in the Los Angeles basin, with sediment S velocities constrained to exceed 0.5 km/s. These constraints are dictated in part by computational limitations. I have shown that the minimum velocity and maximum resolved frequency that I used are compatible, in the sense that clamping V_s at 0.5 m/s has only minimal effect on the peak ground velocity predictions in my frequency band. However, further reduction in $V_s{}^{min}$ would be necessary to include shorter period waves in the analysis. This increase in bandwidth may become critical in order to achieve substantial further refinement in the Q model, since Q may well be a function of frequency. In addition, the accuracy of my results rely on the resolution of the SCEC Reference Velocity Model (Magistrale et al., 2000) used in the simulations. For example, it is possible that my preferred Q_s/V_s relations are biased by error in the velocity or density structure of some basin margins, where significant parts of the attenuation-prone surface waves are generated. Therefore, my Q model should be regarded as provisional and will require revision in parallel with improvements to the elastic structure. However, the velocity model is representative of the current state of the art for characterizing regional structure in 3D simulations, and combining it with my provisional Q model is likely to provide an

improved predictive capability. This expectation can and should be tested in the future using additional earthquake records. Finally, a limitation of the study is that the results may not be easily extrapolated to the sediments of other geological settings. The applicability of the proposed Q_s/V_s relations should be tested before being applied to sedimentary basins in other areas.

In many of the studies reporting observed values of Q_s and Q_p discussed in the Introduction, measurements of V_s are also available. While the geological settings for the different study areas vary tremendously, it is possible to compare the range of Q_s/V_s from observations to those from my simulations. The ranges of Q_s/V_s (V_s in m/s) ratios from observations for material with V_s <1.5 km/s, where the strongest constraints are provided by the modeling, are 0.01-0.041 (Cajon), 0.016-0.035 (Garner Valley), 0.021-0.056 (Santa Clara Valley), and 0.003-0.03 (Parkfield). These values, as well as the empirical power law between Q_s and V_s for San Onofre nuclear generating station, are all in good agreement with my preferred value for Q_s/V_s of 0.02 from modeling. The relation for San Onofre (Q_s=$0.0053V_s{}^{1.25}$, V_s in m/s) gives 12.6 for V_s=500 m/s, similar to the value (10) estimated from Q_s=$0.02V_s$ (m/s), and gives a superlinear increase of Q_s with V_s, similar to Q_s/V_s=0.1 for $V_s > 1.5$ km/s estimated here.

Our results were obtained in the context of a frequency-independent Q model, implemented computationally using the coarse-grained memory variables method (Day, 1998; Day and Bradley 2001). I limited this initial study to frequency-independent models because I thought it unlikely existing data would be able to discriminate among competing models for the frequency-dependence. However, the coarse-grained method can accommodate alternative models for the frequency-dependence of Q, such as general power laws. Simpler computational methods without memory variables could be used in certain special cases (e.g., Graves, 1996, for the special case of Q proportional to frequency).

Our results for the Northridge earthquake have been obtained exclusively through linear models. Laboratory testing of soils in cyclic shear reveals appreciable nonlinear, strain-amplitude-dependent damping for strains exceeding roughly 10^{-4} for high-plasticity-index soils, and roughly 10^{-5} forlow-plasticity-index soils (e.g., Vucetic, 1994). Several recent studies (e.g., Field et al., 1997, 1998; Jones and Olsen, 1998) have attempted to predict the non-linear soil behavior of specific soil sites within the basin, for the Northridge earthquake. These studies generally find significant unrecoverable effects for strains greater than about 10^{-4}; however, the nonlinearity occurs almost exclusively for frequencies above 0.5-1 Hz. In order to assess the degree to which non-linear soil behavior may have affected the results in my study, I have calculated the maximum area-wide shear strain, approximated as the maximum calculated horizontal particle velocity divided by the material S-wave velocity (Figure 9). The strains in the epicentral area exceed the threshold for non-linear behavior, in agreement with Field et al. (1997, 1998); however, the values for the LA basin, where effects of the Q model were most significant, remain in the linear regime for most soils. An exception might be for some very low-plasticity soils, for which the strain levels may be high enough to increase the critical damping ratio by at most a factor of 2 or so above the linear level (Vucetic, 1994), corresponding to a Q reduction of a factor of 2. Therefore, we believe that my Q estimates principally reflect linearly anelastic losses, with the possibility of some modest enhancement, due to nonlinearity in the shallowest part of the model. The latter could affect some very shallow Q_s estimates only, and those probably by less than a factor of 2.

The LA Basin Q_s values in my preferred model are as low as $\approx$10 (see Figure 6) in the near surface. While this value is comparable with many of the seismically inferred shallow Q_s values cited in the Introduction, it is lower, by about a factor of two or more, than most Q_s

laboratory measurements for soils at low strain (e.g., Vucetic, 1994). Part of the discrepancy may be made up for by nonlinearity, although for the reasons noted in the last paragraph, this effect seems unlikely to account for the full discrepancy. Alternatively, it is conceivable that the in situ damping behavior of the LA Basin soils is not well represented by typical laboratory-scale experiments. However, a more likely alternative to explanations based on nonlinearity or scale-dependence of the damping properties is that my inferred Q_s values subsume an additional component of energy loss due to scattering. Such losses would be expected from scattering due to variations in elastic structure occurring at a scale below the resolution of the SCEC model.

Conclusions

Accurate estimation of earthquake ground motion in the Los Angeles Basin, in the 0-0.5 Hz band, using 3D numerical simulations, requires that (i) S-wave velocities as low as at least 0.5 km/s be retained in the velocity model, and (ii) anelastic losses be included, with Q_s/V_s (with V_s in m/s) as low as $\approx$0.02, at least in the uppermost part of the basin where $V_s <$ 1-2 km/s. A model with these features reduces the standard deviation of the residuals between synthetic and observed natural log of peak velocities from 1.13 to 0.26, relative to a lossless model with the same seismic velocity structure. In contrast, the ground motion simulations are relatively insensitive to Q_p. The most important effect of the attenuation model is in reducing the amplitudes of surface waves propagating within the basin sediments. The inferred Q_s values are sufficiently low, compared with typical low-strain laboratory measurements of soil damping, that it is likely that they reflect combined effects of both intrinsic anelastic attenuation and scattering attenuation due to unmodeled heterogeneity in the seismic velocity structure. The Q estimates from this study may serve as a valuable starting point for future development of improved models of regional anelastic structure. Those efforts would benefit from including higher frequencies, modeling lower seismic velocities, and exploiting data from multiple earthquakes.

The optimal Q model was used to construct site amplification maps for the Los Angeles basin for seven earthquake scenarios (M 6.75 earthquakes on the Palos Verdes, Elysian Park, Santa Monica, Newport-Inglewood faults, approximations to the M 6.7 1994 Northridge, the M 6.4 1933 Long Beach, and the M 5.9 1987 Whittier-Narrows events), measured as 3D/1D 0-0.5 Hz peak velocity ratios. The individual scenarios show amplification of peak velocities up to an order of magnitude relative to the background model. The distribution of mean peak velocity ratios, as calculated from the seven scenarios, has a maximum of 5.1. In general, both the individual scenarios and their mean values show that the largest amplifications occur above the deepest parts of the basin and above the steeply-dipping basin boundaries. The largest mean amplification is furthermore associated with relatively small uncertainties. The largest uncertainties of the mean amplification above the basin (log standard deviation >1) are associated with sites in the southern part of SFV, northwest of SFV, and near Pasadena. For the seven scenario earthquakes, the amplification tends to increase with distance from the causative fault to the basin structure. It is possible that this pattern is due to stronger amplification of the more complex wavefield impinging onto the basin structure from the distant earthquakes compared to that of the predominant body waves from nearby earthquakes. The amplification is caused by a combination of effects from the 3D basin structure and differences in impedance between the 1D and 3D models. The maximum amplification averaged over sites above similar basin structure for the scenario earthquakes is 11.6, associated with sites located above the deeper part of the basin.

Acknowledgements

The computations were carried out on SGI Origin 2000 computers at Los Alamos and MRL (NSF Grant CDA 96-01954), and on the SUN Enterprise, ICS, UCSB.

Publications Produced by This Award

Olsen, K.B., S.M. Day, and C.R. Bradley (2002). Estimation of Q for long-period (>2 s) waves in the Los Angeles Basin, *Bull. Seis. Soc. Am.*, revised for publication.

References

Abercrombie, R. (1997). Near-surface attenuation and site effects from comparison of surface and deep borehole recordings, *Bull. Seis. Soc. Am.* **87**, 731-744.

Archuleta, R.J., S.H. Seale, P.V. Sangas, L.M. Baker, and S.T. Swain (1992). Garner Valley downhole array of accelerometers: instrumentation and preliminary data analysis, *Bull. Seis. Soc. Am.* **82**, 1592-1621.

Aster, R. and P.M. Shearer (1991). High-frequency borehole seismograms recorded in the San Jacinto fault zone, southern California: Part 2. Attenuation and site effects, *Bull. Seis. Soc. Am.* **81**, 1081-1100.

Bardet, J.P. and C. Davis (1996). Engineering observations on ground motion at the Van Norman Complex after the 1994 Northridge earthquake, *Bull. Seism. Soc. Am.*, **86**, No. 1B, S333-S349.

Blanch, J.O., J.O.A. Robertsson, and W.W. Symes (1995). Modeling of a constant Q: methodology and algorithm for an efficient and optimally inexpensive viscoelastic technique, *Geophysics* **60**, 176-184.

Cerjan, C., D. Kosloff, R. Kosloff, and M. Reshef (1985). A nonreflecting boundary condition for discrete acoustic and elastic wave equations, *Geophysics* **50**, 705-708.

Chen, K-C., J-M. Chiu, and Y-T. Yang (1994). $Q_p - Q_s$ relations in the sedimentary basin of the upper Mississippi Embayment using converted phases, *Bull. Seis. Soc. Am.* **84**, 1861-1868.

Clayton, R. and B. Engquist (1977). Absorbing boundary conditions for acoustic and elastic wave equations, *Bull. Seism. Soc. Am.* **67**, 1529-1540.

Day, S.M. (1996). RMS response of a one-dimensional halfspace to SH, *Bull. Seism. Soc. Am.* **86**, 363-370.

Day, S.M. (1998). Efficient simulation of constant Q using coarse-grained memory variables, *Bull. Seism. Soc. Am.* **88**, 1051-1062.

Day, S.M., and C. Bradley (2001). Memory-efficient simulation of anelastic wave propagation, *Bull. Seism. Soc. Am.* **91**, 520-531.

Dolan, J. J., K. Sieh, T. K. Rockwell, R. S. Yeats, J. Shaw, J. Suppe, G. J. Huftile, and E. M. Gath (1995). Prospects for larger or more frequent earthquakes in the Los Angeles Metropolitan region, *Science* **267**, 199-205.

Faust, L.Y. (1951). Seismic velocity as a function of depth and geologic time, *Geophysics* **16**, 192-206.

Field, E.H., P.A. Johnson, I.A. Beresnev, and Y. Zeng (1997). Nonlinear ground-motion amplification by sediments during the 1994 Northridge earthquake, *Nature* **390**, 599-602.

Field, E.H., Y. Zeng, P.A. Johnson, and I.A. Beresnev (1998). Nonlinear sediment response during the 1994 Northridge earthquake: Observations and finite source simulations, *Jour. Geophys. Res.* **103**, 26,869-26,883.

Graves, R.W. (1996). Simulating seismic wave propagation in 3D elastic media using staggered-grid finite differences, *Bull. Seism. Soc. Am.* **86**, 1091-1106.

Gibbs, J.F., D.M. Boore, W.B. Joyner, and T.E. Fumal (1994). The attenuation of seismic shear waves in Quaternary alluvium in Santa Clara Valley, California, *Bull. Seis. Soc. Am.* **84**, 76-90.

Hauksson, E., T-L. Teng, and T.L. Henyey (1987). Results from a 1500 m deep, three-level downhole seismometer array: site response, low Q values, and f_{max}, *Bull. Seis. Soc. Am.* **84**, 1883-1904.

Hauksson (2000). Crustal structure and seismicity distribution adjacent to the Pacific and North America plate boundary in Southern California, *Jour. Geophys. Res.* **105**, 13,875-13,903.

Jones, E., and K.B. Olsen (1998). Modeling of non-linear soil response from earthquakes in Los Angeles, *SRL* **69**, 148.

Jongmans, D. and P.E. Malin (1995). Vertical profiling of microearthquake S waves in the Varian well at Parkfield, California, *Bull. Seis. Soc. Am.* **85**, 1805-1820.

Hadley, D. and H. Kanamori (1977). Seismic structure of the Transverse Ranges, California, *Geol. Soc. Am. Bull.* **88**, 1469-1478.

Hough, S.E., C. Dietel, G. Glassmoyer, and E. Sembera (1995). On the variability of after-shock ground motions in the San Fernando Valley, *Geophys. Res. Lett.* **22**, 727-730.

Levander, A. R. (1988). Fourth-order finite-difference P-SV seismograms, *Geophysics* **53**, 1425-1436.

Ludwig, W.J., J.E. Nafe and C.L. Drake (1970). Seismic refraction, in The Sea, 4, A.E. Maxwell, ed., p. 53-84, Wiley-Interscience, New York, New York.

Magistrale, H., S. Day, R. Clayton, and R. Graves (2000). The SCEC Southern California reference three-dimensional seismic velocity model Version 2, *Bull. Seism. Soc. Am.* **90**, S65-S76.

Malin, P.E., J.A. Waller, R.D. Borcherdt, E. Cranswick, E.G. Jensen, and J. Van Schaack (1988). Vertical seismic profiling of Oroville microearthquakes: velocity spectra and particle motion as a function of depth, *Bull. Seis. Soc. Am.* **78**, 401-420.

Moczo, P., J. Kristek, R.J. Archuleta, and L. Halada (2002). 3D staggered-grid finite-difference modeling with volume harmonic and arithmetic averaging of elastic moduli and densities, *Bull. Seism. Soc. Am.*, submitted.

Nafe, J.E. and C.L. Drake (1960). Physical properties of marine sediments, in The Sea 3, M.N. Hill, Ed., Interscience, New York, New York, 794-815.

Olsen, K.B. (1994). Simulation of three-dimensional wave propagation in the Salt Lake Basin, *Ph.D. Thesis*, University of Utah, Salt Lake City, Utah, 157 p.

Olsen, K.B., and G.T. Schuster (1995). Causes of low-frequency ground motion amplification in the Salt Lake Basin: The case of the vertically-incident P wave, *Geophys. J. Int.* **122**, 1045-1061.

Olsen, K.B., and R.J. Archuleta (1996). Three-dimensional simulation of earthquakes on the Los Angeles Fault System, *Bull. Seism. Soc. Am.* **86**, 575-596.

Olsen, K.B., J.C. Pechmann, and G.T. Schuster (1995a). Simulation of 3-D elastic wave propagation in the Salt Lake Basin, *Bull. Seism. Soc. Am.* **85**, 1688-1710.

Olsen, K.B., R.J. Archuleta, and J.R. Matarese (1995b). Three-dimensional simulation of a magnitude 7.75 earthquake on the San Andreas fault in southern California, *Science* **270**, 1628-1632.

Olsen, K.B., R. Nigbor, and T. Konno (2000). 3D viscoelastic wave propagation in the Upper Borrego Valley, California, constrained by borehole and surface data, *Bull. Seis. Soc. Am.* **90**, 134-150.

Olsen, K.B. (2000). Site amplification in the Los Angeles basin from 3D modeling of ground motion, *Bull. Seis. Soc. Am.* **90**, S77-S94.

Robertsson, J.O.A., J.O. Blanch, and W.W. Symes (1994). Viscoelastic finite-difference modeling, *Geophysics* **59**, 1444-1456.

Sato, H., and M.C. Fehler (1998). Seismic wave propagation and scattering in the heterogeneous Earth, AIP Series in Modern Acoustics and Signal Processing **7**, (Monograph) 308 pp.

Seale, S., and R.J. Archuleta (1989). Site amplification and attenuation of strong ground motion, *Bull. Seis. Soc. Am.* **79**, 1673-1696.

Vucetic, M. (1994). Cyclic threshold shear strains in soils, *Journal of Geotechnical Engineering*, **120**, 2208-2228.

Wald, D.J. and R.W. Graves (1998). The seismic response of the Los Angeles basin, California, *Bull. Seism. Soc. Am.* **88**, 337-356.

Wald, D.J., T.H. Heaton, and K.W. Hudnut (1996). The slip history of the 1994 Northridge, California, earthquake determined from strong motion, teleseismic, GPS, and levelling data, *Bull. Seism. Soc. Am.* **86**, S49-S70.

Wiggens, R. A., G. A. Frazier, J. Sweet, and R. Apsel (1978). Modeling strong motions from major earthquakes, Proceedings of the Second International Conference on Microzonation for Safer Construction – Research and Application, San Francisco, California, November 26-Dec 1 1978, 693-700.

Wills, C.J., M. Petersen, W.A. Bryant, M. Reichle, G.J. Saucedo, S. Tan, G. Taylor, and J. Treiman (2000). A site-conditions map for California based on Geology and Shear-wave velocity, *Bull. Seism. Soc. Am.* **86**, S187-S208.

Zhu, L. and H. Kanamori (2000). Moho depth variation in Southern California from teleseismic receiver functions, *Jour. Geophys. res.* **105**, 2969-2980.

Table 1. Earthquake Rupture Parameters

	Hypocenter Longitude, Latitude, Depth (km)	Fault Width, Length, Depth to Top (km)	Dip	Strike	Rake	Moment Magnitude
NR	-118.53, 34.205, 17.6	24, 18, 6.0	40	122	101	6.7
EP	-118.205, 34.102, 14.8	21, 16, 10.5	25	302	90	6.75
SM	-118.643, 34.065, 10.4	17, 37, 0.4	65	260	90	6.75
PV	-118.332, 33.781, 7.2	16, 35, 0.4	90	141	180	6.75
WN	-118.072, 34.049, 14.4	0.4, 0.4, 7.0	27	270	90	5.9
LB	-117.99, 33.655, 9.6	10, 18. 0.4	90	133	180	6.4
NI	-118.237, 33.885, 7.6	15, 41, 0.4	90	138	180	6.75

Table 2. 3-D Modeling Parameters

Spatial discretization (km)	0.2
Temporal discretization (sec)	0.0125
Lowest P-wave velocity (km/sec)	0.936
Lowest S-wave velocity (km/sec)	0.5
Lowest Density (kg/m^3)	1700
Rupture Velocity (m/s)	3000
Number of timesteps	10000
Simulation time (sec)	120

Table 3. Standard Deviation of the Natural Log Peak Velocity Misfit

V_s^{min} (km)	Q_s/V_s	Q_p/Q_s	V_s^T (km/s)	Deep Basin	All
1.0	∞	1	∞	0.75	0.74
0.5	∞	1	∞	1.13	0.79
0.5	0.1	1.5	∞	0.77	0.59
0.5	0.05	1.5	∞	0.51	0.51
0.5	0.02	1.5	∞	0.33	0.62
0.5	0.02	1.5	2	0.27	0.54
0.5	0.02	1.5	1.5	0.27	0.53
0.5	0.02	1.5	1	0.33	0.48
0.5	0.02	$(3/4)(V_p/V_s)^2$	2	0.26	0.53

Figure Captions

Figure 1. Topographic map of the Los Angeles area model. The rectangle depicts the modeling area. The dashed line shows the surface projection of the fault for the 1994 Northridge earthquake.

Figure 2. 3D image of the isosurface for an S-wave velocity of 2.5 km/s of the SCEC velocity model version 2. The thin solid lines depict major freeways in the modeling area and the thick solid line is the coastline.

Figure 3. (top) 150 m depth contour for the isosurface V_s=0.5 km/s and (bottom) 850 m depth contour for the isosurface V_s=1.0 km/s of the SCEC velocity model version 2. The thin solid lines depict major freeways in the modeling area and the thick solid line is the coastline. The maximum depth of the isosurface is 300 m.

Figure 4. Difference between the natural log of the observed and synthetic peak velocities at 55 sites, represented by the length of the bars; blue depicts underprediction, red depicts overprediction. (a) Lossless model, V_s^{min}=1 km/s, (b) lossless model, V_s^{min}=0.5 km/s, (c) Q_s/V_s=0.1, (d) Q_s/V_s=0.5, and (e) Q_s/V_s=0.02. Q_s/V_s=0.02 for (f) V_s <1.0 km/s, (g) V_s <1.5 km/s, (h) and (i) V_s <2.0 km/s. (c) - (h) use Q_p/Q_s=1.5 (Q_p^1), (i) uses $Q_p/Q_s = (3/4)(V_p/V_s)^2$ (Q_p^2). The thin solid lines depict major freeways in the modeling area and the thick solid line is the coastline.

Figure 5. Illustration of the variation of Q_s for the Q_s/V_s relations used in Figure 4b-d at the deep basin site IGU (see Figure 6 for location).

Figure 6. (a) Comparison of observed versus synthetic 0.1-0.5 Hz waveforms for our preferred Q model as well as the elastic response (thin traces) at 13 sites within the model. "O" and "S" depict observed and synthetic seismograms, respectively, and "Z", "1" and "2" depict vertical, 122^o and 32^o horizontal components, respectively.

Figure 7. Comparison of elastic (thin traces) and preferred viscoelastic synthetic seismograms at (top) JFP and (bottom) IGU.

Figure 8. Peak velocities in the LA basin for the simulation using Q_s/V_s=0.02 for V_s <1.5 km/s and Q_s/V_s=0.1 for V_s >1.5 km/s, and Q_p/Q_s=1.5.

Figure 9. Estimate of the peak horizontal strains in the LA basin for the simulation using Q_s/V_s=0.02 for V_s <1.5 km/s and Q_s/V_s=0.1 for V_s >1.5 km/s, and Q_p/Q_s=1.5. The strains are calculated as the peak horizontal velocities divided by the surface V_s.

Figure 10. Maps of 3D/1D 0-0.5 Hz peak velocity ratios for 7 scenarios. The thin white lines show major freeways in the Los Angeles area. The thick white line is the coastline. The range of amplification values is listed for each scenario.

Figure 11. Maps of the 3D/1D 0-0.5 Hz peak velocity ratios and their uncertainties. Mean values (top left) and max values (top right), and the standard deviation of the natural log of the amplification (bottom left). The thin lines show major freeways in the area. The bottom right figure shows the isosurface for an S-wave velocity of 2.5 km/s.

Figure 12. 3D/1D 0-0.5 Hz peak velocity ratios for the 7 scenarios, as well as their mean and log standard deviation, averaged for sites with common depth to the isosurface for an S-wave velocity of 2.5 km/s.

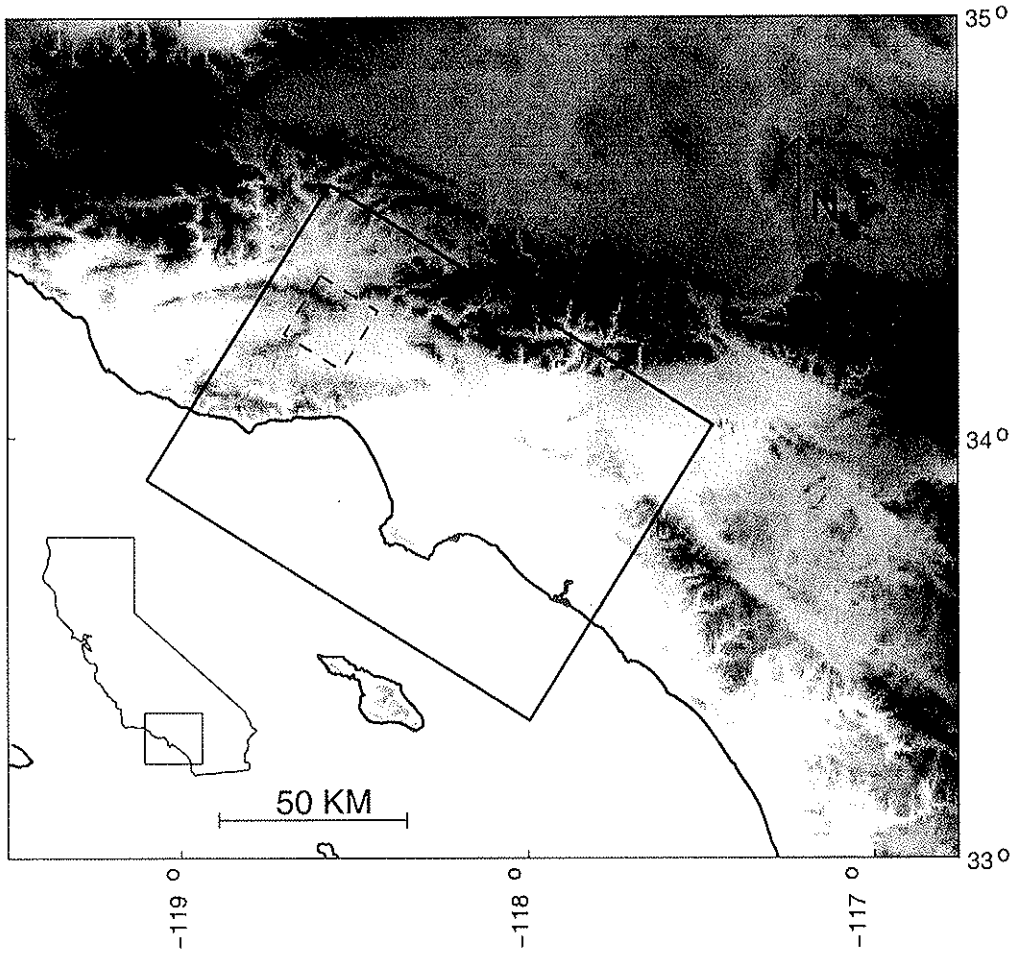

Figure 1:

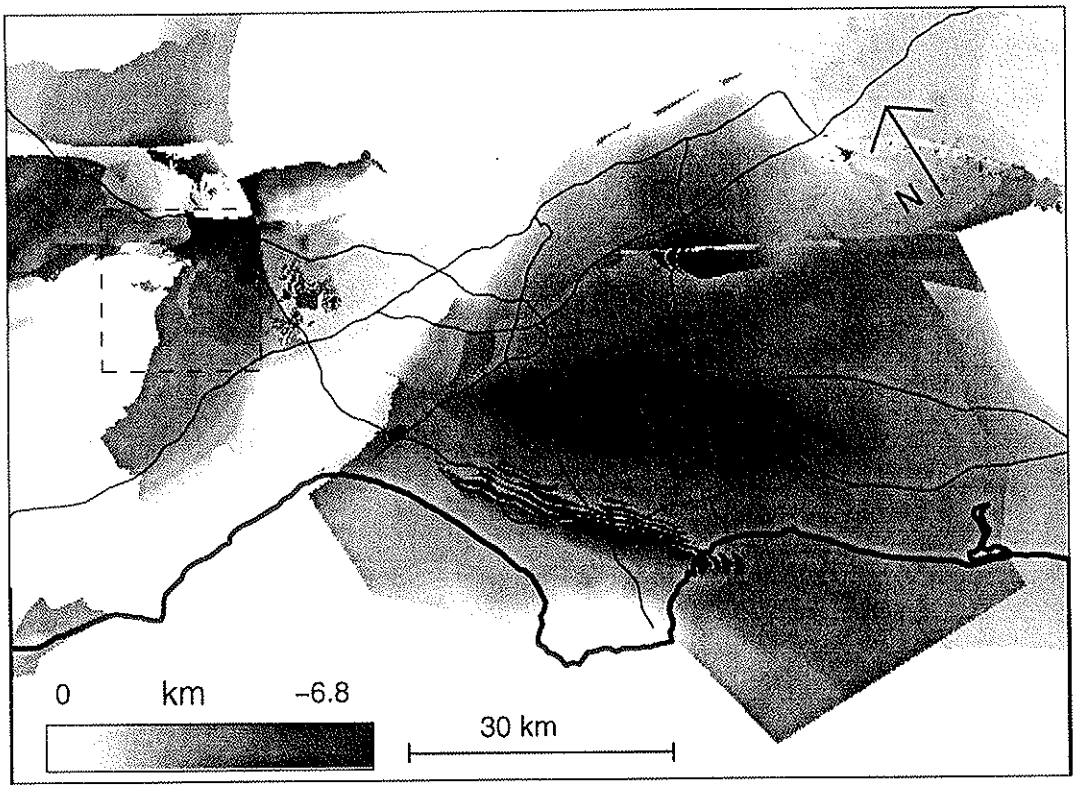

Figure 2:

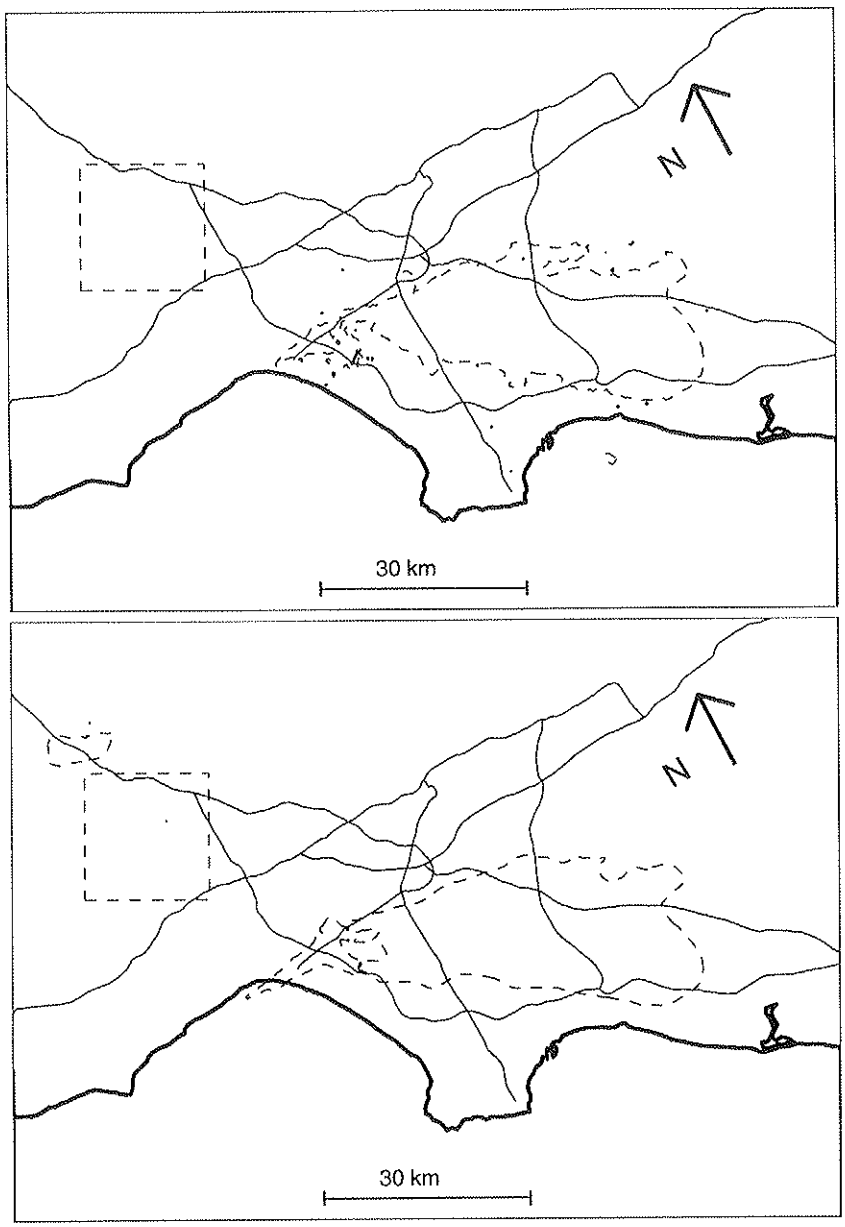

Figure 3:

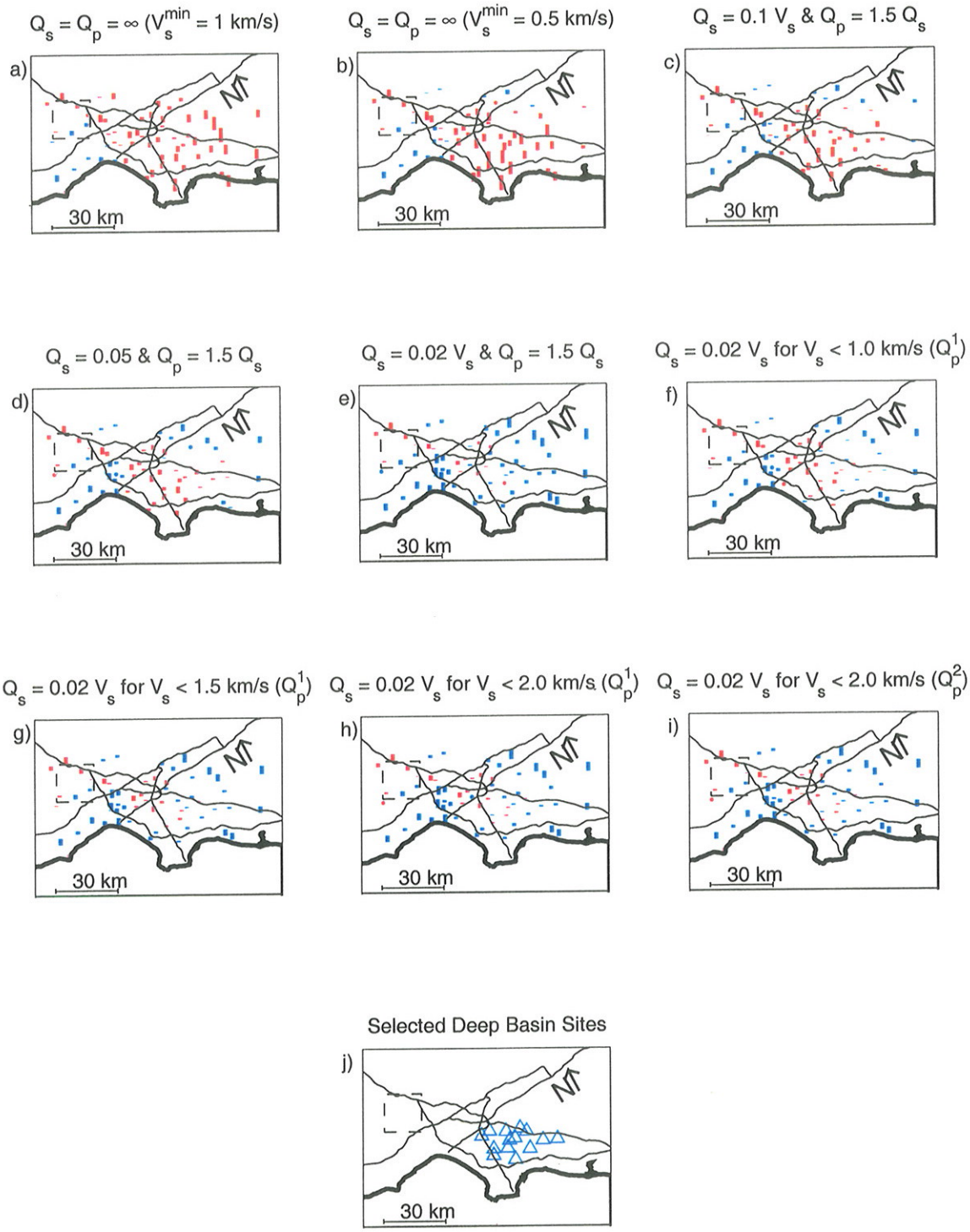
$Q_s = Q_p = \infty$ (V_s^{min} = 1 km/s)
a)
30 km
$Q_s = Q_p = \infty$ (V_s^{min} = 0.5 km/s)
b)
30 km
Q_s = 0.1 V_s & Q_p = 1.5 Q_s
c)
30 km
Q_s = 0.05 & Q_p = 1.5 Q_s
d)
30 km
Q_s = 0.02 V_s & Q_p = 1.5 Q_s
e)
30 km
Q_s = 0.02 V_s for V_s < 1.0 km/s (Q_p^1)
f)
30 km
Q_s = 0.02 V_s for V_s < 1.5 km/s (Q_p^1)
g)
30 km
Q_s = 0.02 V_s for V_s < 2.0 km/s (Q_p^1)
h)
30 km
Q_s = 0.02 V_s for V_s < 2.0 km/s (Q_p^2)
i)
30 km
Selected Deep Basin Sites
j)
30 km

Figure 4:

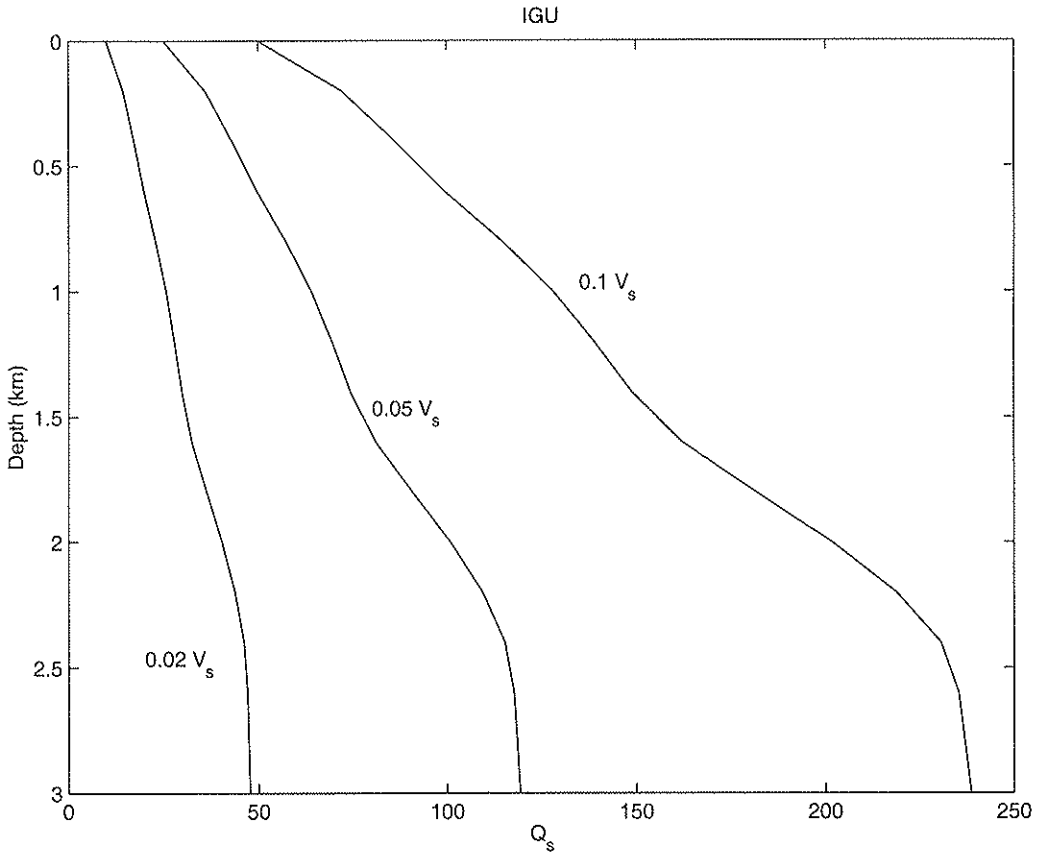
IGU
Depth (km)
0
0.5
1
1.5
2
2.5
3
0
50
100
150
200
250
Q_s
0.1 V_s
0.05 V_s
0.02 V_s

Figure 5:

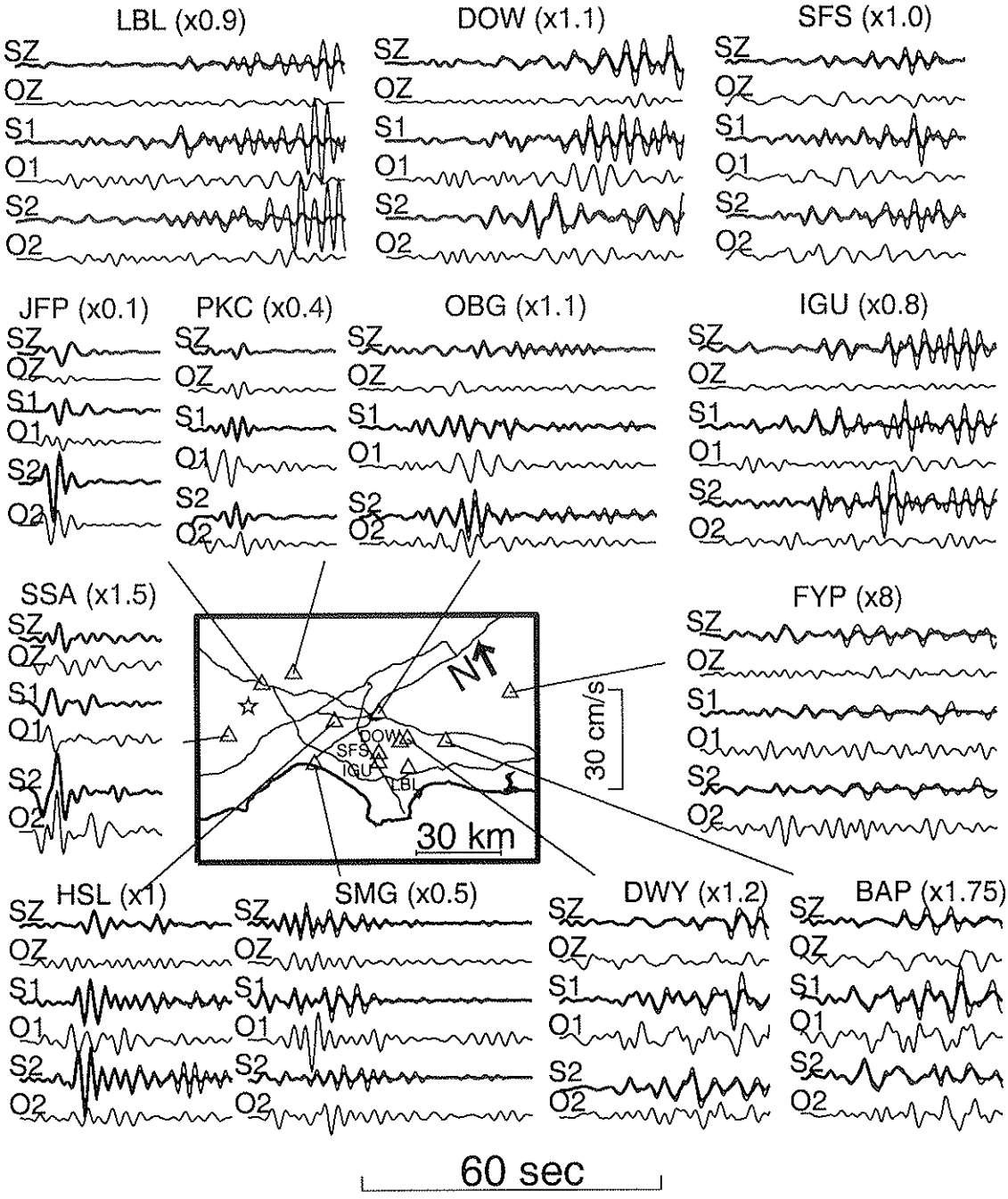
LBL (x0.9)
DOW (x1.1)
SFS (x1.0)
SZ
OZ
S1
O1
S2
O2
JFP (x0.1)
PKC (x0.4)
OBG (x1.1)
IGU (x0.8)
SSA (x1.5)
FYP (x8)
N
DOW
SFS
IGU
LBL
30 km
30 cm/s
HSL (x1)
SMG (x0.5)
DWY (x1.2)
BAP (x1.75)
60 sec

Figure 6:

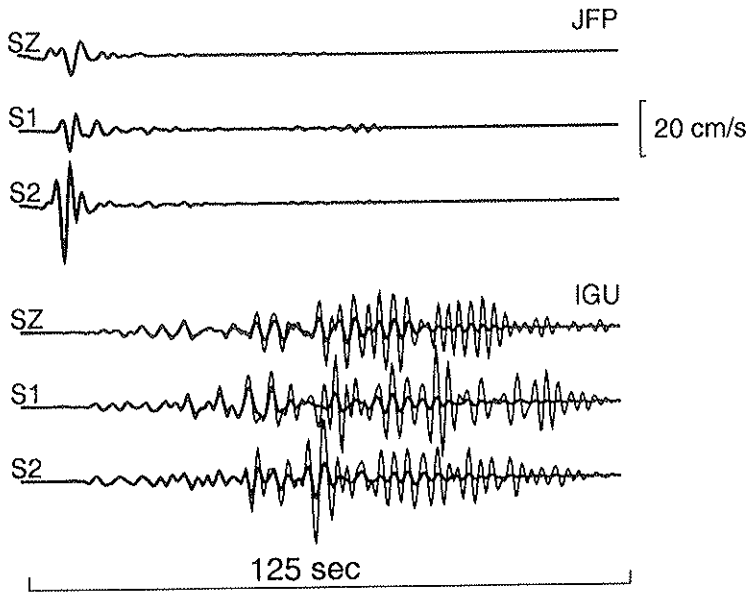

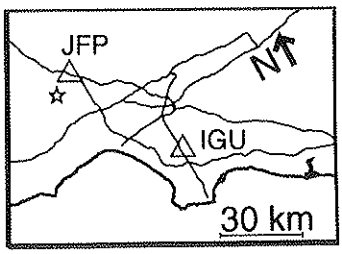

Figure 7:

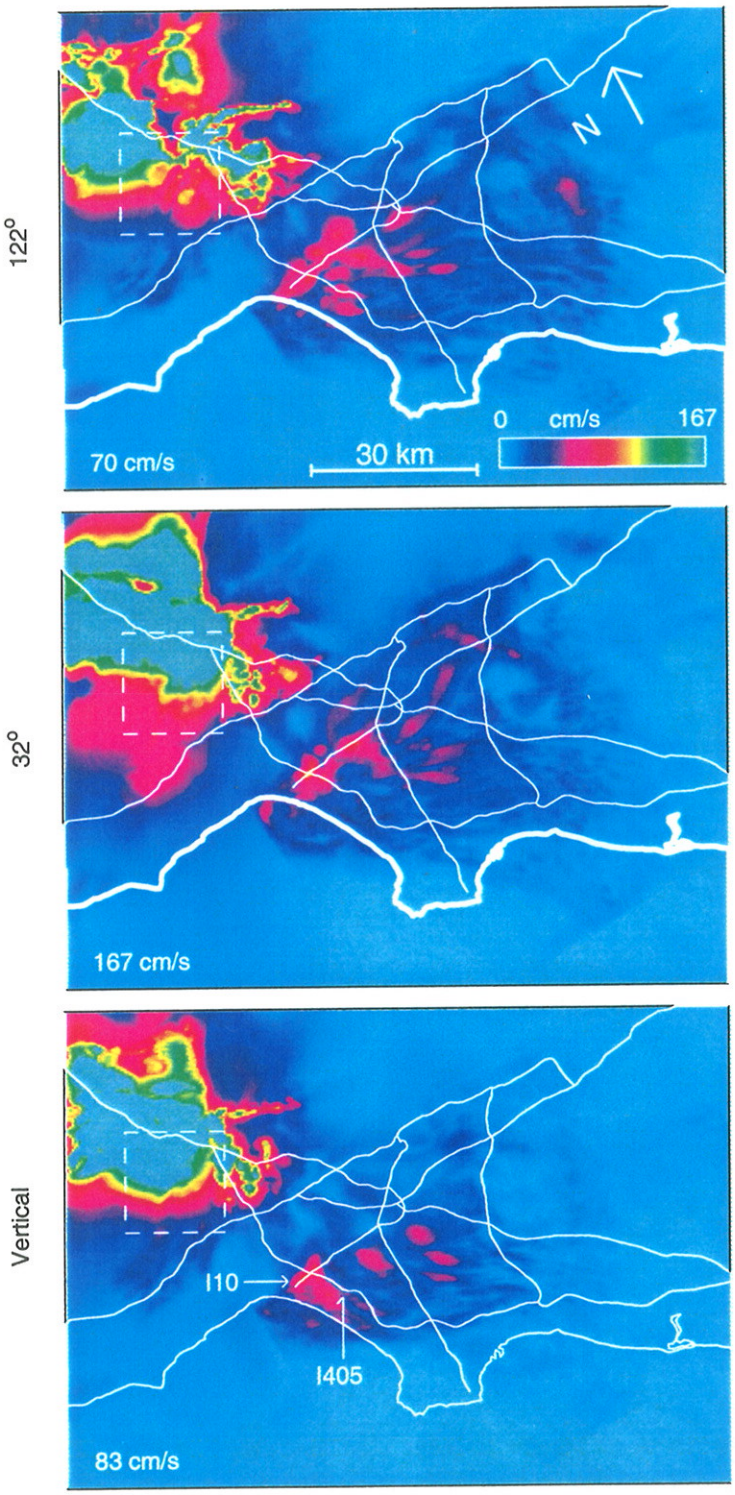

Figure 8:

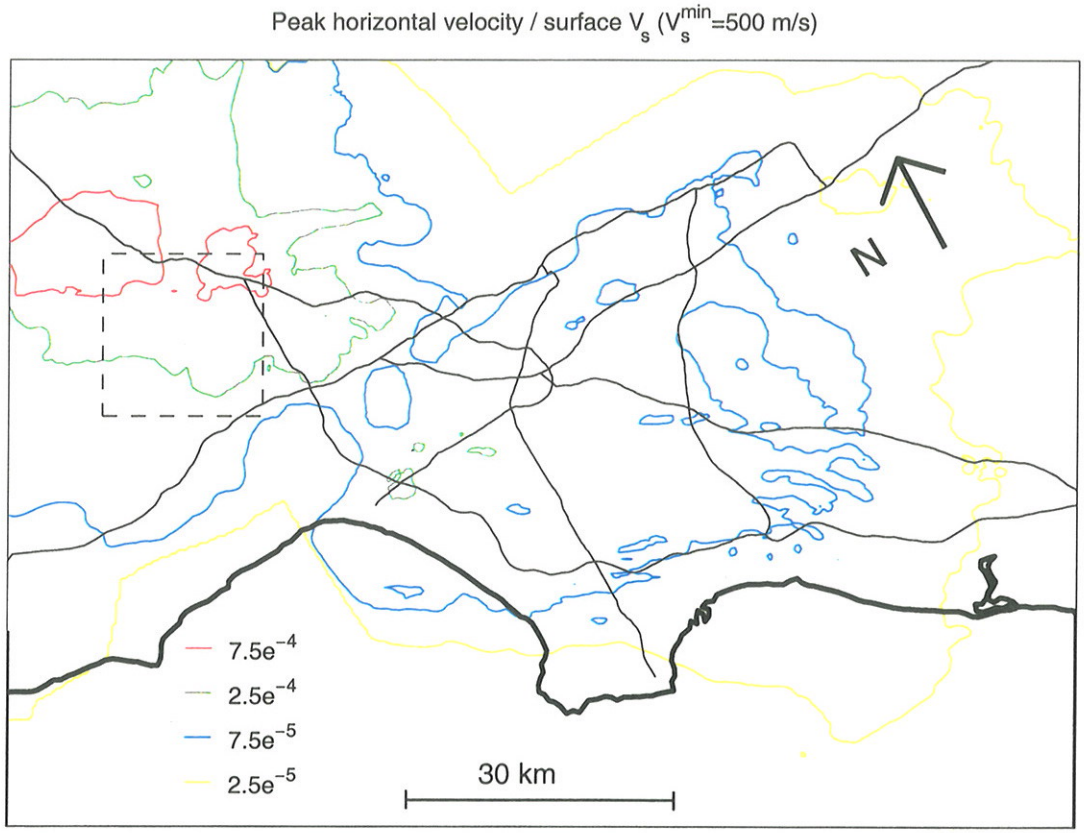
Peak horizontal velocity / surface V_s (V_s^{min}=500 m/s)
N
7.5e^{-4}
2.5e^{-4}
7.5e^{-5}
2.5e^{-5}
30 km

Figure 9: